Understanding Catalytic Activity Trends of Electrochemical Ammonia Oxidation Reaction using Density Functional Theory Calculations and Microkinetic Modeling

Ho Yeon Jang and Seoin Back[*]

AUTHOR ADDRESS

Department of Chemical and Biomolecular Engineering, Institute of Emergent Materials, Sogang University, Seoul 04107, Republic of Korea

AUTHOR INFORMATION

Corresponding Author

E-mail: sback@sogang.ac.kr (SB)

ABSTRACT

Electrochemical ammonia oxidation reaction (AOR) is promising as an alternative anodic reaction to oxygen evolution in water electrolysis system. Herein, we develop a microkinetic model based on density functional theory (DFT) calculations for all possible reaction pathways considering both thermochemical and electrochemical N-N bond formation processes. From the microkinetic analysis, we discover that Faradaic bond formation contributes to AOR more significantly than non-Faradaic counterpart and we observe good agreements with the experimental results. We then construct a kinetic volcano plot using binding energies of two reaction intermediates as descriptors, which suggests a catalyst design strategy. Following this strategy, we enumerate numerous alloy combinations and identify a few promising candidates with higher catalytic activity than the most active monometallic Pt catalyst.

KEYWORDS

1. Introduction

Toward a sustainable energy cycle, H_2 economy has been considered as one of the most promising solutions to overcome drawbacks of the current fossil fuel economy since it does not emit any pollutants or greenhouse gases during conversion processes[1, 2]. However, 96 % of the current H_2 production relies on thermochemical conversions of carbon-based fuels via pyrolysis, gasification and steam reforming of natural gas, requiring clean alternative methods[2, 3]. Water electrolysis has been investigated to produce green H_2, which consists of H_2 evolution reaction (HER) at the cathode and O_2 evolution reaction (OER) at the anode[4]. While the cathodic reaction is considerably facile and various types of catalysts could be employed, the anodic reaction suffers from large overpotentials and harsh operating conditions, requiring noble metal-based oxide catalysts such as Ir and Ru oxides[5, 6]. As an alternative anodic reaction, electrochemical ammonia (NH_3) oxidation reaction (AOR) has several advantages over OER[7]. The operating potential (< 1 V_{RHE}) of AOR is much lower than that of OER (> 1.5 V_{RHE}), thus catalyst materials are not limited to oxides as in OER. In addition, the equilibrium potential for N_2/NH_3 is 0.06 V_{RHE}, indicating that, when coupled with HER, theoretically 95 % less electrical energy is required compared to OER of which the equilibrium potential is 1.23 V_{RHE}[8, 9].

Pt and Pt-based alloys have demonstrated catalytic responses for AOR[10-14]. Katan and Galiotto evaluated Pt black for anodic AOR, where they observed the current efficiency of nearly 100 % for N_2 production[10]. Vidal-Iglesias *et al.* analyzed structure sensitivity of polycrystalline Pt[12], where they found that Pt (100) facet showed strong NH_3 oxidation peak at 0.57 V_{RHE}, while relatively small oxidation peaks were observed at potentials higher than 0.8 V_{RHE} and lower than 0.6 V_{RHE} for (110) and (111), respectively. To further improve the catalytic activity of Pt catalysts, Vitse *et al.* investigated bimetallic alloys of Pt-Ir and Pt-Ru,[13] where they observed a

reduction in overpotentials to achieve the current density of ~70 mA cm^{-2} for Pt-Ir (0.36 V) compared to Pt (0.56 V). Mishima et al. also examined Pt-Ir alloy using cyclic voltammetry and differential electrochemical spectroscopy (DEMS)[15], and they observed that Pt-Ir exclusively produced N$_2$ and NO at low (0.40 ~ 0.80 V$_{RHE}$) and high (above 0.80 V$_{RHE}$) potentials, respectively. A systematic study was performed by De Vooys et al.[16] for a series of reactive transition metals (Pt, Pd, Rh, Ru, and Ir) and coinage metals (Ag, Au, Cu) in alkaline conditions using voltammetry and DEMS. They suggested that Pt and Ir achieved the best catalytic activities due to moderate adsorption energies of atomic nitrogen (N*). It was proposed that the transition metals with strong N* affinity such as Ru, Rh, and Pd are not suitable for AOR, since adsorbed NH$_x$* species readily get deprotonated to N* leading to kinetically sluggish N-N coupling, while weak N* affinity of the coinage metals prevents a facile NH$_3$ activation.

Using density functional theory (DFT) calculations, Herron et al. investigated catalytic activities of AOR on the most close-packed surfaces (e.g., (111) facet of face-centered cubic (FCC) metals) of 12 transition metals[9], where they considered reaction mechanisms involving two non-Faradaic N-N bond coupling processes of adsorbates: (1) Gerischer and Mauer (GM) mechanism[17], where adsorbed NH$_x$ species (NH$_x$*) form N-N bond (NH$_x$* + NH$_y$* → N$_2$H$_{x+y}$*) and (2) NN mechanism, where two fully deprotonated N* form N-N bond (N* + N* → N$_2$*). Generally, GM mechanism was found to be kinetically more facile compared to NN mechanism. By calculating the electrochemical limiting potentials (U$_L$) and activation energies (G$_{a,i}$) of N-N coupling processes, they concluded that Pt is the most active metal followed by Ir, which is in agreement with the previous experiments[16]. Recently, Elnabawy et al. performed a similar analysis on more open (100) facet of 8 FCC transition metals to understand the effect of facets on AOR[18]. The activation energy of N-N bond formation through the coupling of two NH$_2$*

($NH_2^* + NH_2^* \rightarrow N_2H_4^*$) on Pt (111) was 1.07 eV, which is lowest among the GM and NN mechanisms. On Pt (100), however, the lowest activation energy of N-N bond formation ($N^* + N^* \rightarrow N_2^*$) was 0.53 eV via NN mechanism, indicating higher AOR activity on Pt (100) compared to Pt (111). It was highlighted that higher catalytic activity of Pt (100) was originated from weaker N^* adsorption energy than Pt (111), which destabilizes reactants, thus facilitates the dimerization of two N^*. We note that only N-N coupling processes via two adsorbates have been considered in AOR in literature and microkinetic modeling that quantitatively predicts results of complex electrochemical AOR has not been reported to date.

In this work, we performed DFT calculations to systematically examine 26 *d*-block transition metals for AOR considering all possible reaction mechanisms. In addition to GM and NN mechanisms, we investigated electrochemical N-N coupling processes. We employed linear scaling relations and Brønsted−Evans−Polanyi (BEP) relations to construct a two-dimensional kinetic volcano plot through the microkinetic modeling. We found that a contribution of electrochemical N-N coupling is more significant than thermochemical GM/NN mechanisms, highlighting the importance of including electrochemical pathways to rationally predict catalytic activities. The microkinetic modeling results confirmed that Pt is the most active monometallic catalyst and provided a design strategy to improve the catalytic activity. Based on the suggested strategy, we screened bimetallic alloys consisting of two metals with different N-affinities and proposed a few alloy combinations ($IrAu_3$, $RhAg_3$, $NiCu_3$, $RhAu_3$, $PtCu_3$, $NiAg_3$, $PdCu_3$ and $NiAu_3$) as more active catalysts than Pt. We expect this work to provide a fundamental understanding and be a basis of developing new active catalysts for AOR.

2. Computational Details

2.1 DFT Calculations

Spin-polarized DFT calculations were performed using VASP code (version 5.4.4.)[19, 20] with Bayesian error estimation functional with van der Waals correlation (BEEF-vdW)[21], which accurately describes chemical and physical interactions. For bulk (slab) relaxations, convergence tolerances for force and energy were set to 0.03 eV/Å (0.05 eV/Å) and 10^{-5} eV (10^{-4} eV), respectively. A kinetic energy cutoff was set to 500 eV (400 eV), and $k_1 \times k_2 \times k_3$ ($k_1 \times k_2 \times 1$) Monkhorst-pack k-point sampling satisfying $a_n \times k_n > 25$ Å was used, where a_n is a length of the unit cell vector[22]. After relaxing 26 d-block bulk structures, we modeled (111) surface for FCC metals (Ag, Au, Cu, Ir, Ni, Pd, Pt, Rh), (110) for BCC metals (Cr, Fe, Mn, Mo, Nb, Ta, V, W) and (0001) for HCP metals (Co, Hf, Os, Re, Ru, Sc, Tc, Ti, Y, Zr). For all slab structures, four-layered (3×3) surfaces were modeled with 20 Å of a vacuum layer added in the z-direction to avoid imaginary interactions between repeating atomic structures (**Figure S1**).

To calculate free energies of electrochemical deprotonation steps, we employed the computational hydrogen electrode (CHE) method, which assumes that the chemical potential of proton and electron pair ($H^+ + e^-$) is equal to that of 0.5 $H_2(g)$ at standard conditions and $U = 0$ V_{RHE}[23]. DFT calculated electronic energies were converted into free energies by adding free energy corrections, *i.e.*, $G = E_{DFT} + ZPE + \int C_p\,dT - TS$, where E_{DFT} is DFT calculated total energy, and ZPE, $\int C_p\,dT$, and TS correspond to zero-point energy, enthalpic, and entropic corrections, respectively. These corrections were calculated using the ideal gas (harmonic) approximation for gas molecules (adsorbates) implemented in Atomic Simulation Environment (ASE)[24] (**Table S1**). An implicit solvation effect was included using VASPsol[25]. We calculated

binding free energies of adsorbates with respect to H_2 and NH_3 molecules **(Supplementary Note 1)**

2.2 Microkinetic Modeling

To predict turnover frequencies (TOF) of AOR, we performed a microkinetic modeling based on the mean-field theory and the steady-state approximation using CatMAP code[26]. For thermochemical N-N bond formation steps, the rate constant is expressed as

$$k_i = \frac{k_B T}{h} \, exp\{-G_{a,i}/k_B T\}$$

where k_B, h and $G_{a,i}$ are Boltzmann constant, Planck constant and activation energy of i th step, respectively, and prefactor ($k_B T/h$) is calculated to be 6.21×10^{12} at T= 298.15 K. To estimate activation energies of thermochemical N-N bond formation steps (GM and NN mechanisms) for all transition metals, we used BEP relations based on the previous DFT results by Herron $et\ al.$[9]. Although the previous study used a different functional (PW91) and did not include the solvation effect, we observed that reaction free energies and activation energies were qualitatively in good agreement **(Figure S2, S3)**. The activation free energies of the thermochemical N-N bond formation steps, $G_{a,i}$, were calculated as follows:

$$G_{a,i} = G_{a,i}^{ref} + \gamma_i(\Delta G_{rxn,i} - \Delta G_{rxn,i}^{ref})$$

where $G_{a,i}$, $\Delta G_{rxn,i}$ and γ_i are activation free energies, reaction free energies and BEP slope for each N-N bond formation step. The superscript 'ref' refers to the calculated values for Pt (111). The $G_{a,i}$ obtained from the BEP relations are summarized in **Table S2**.

For electrochemical N-N coupling steps, the rate constant of the i th step is calculated as

$$k_i = A_i \, exp\{-G_{a,i}/k_B T\}$$

where A_i corresponds to the effective prefactor (1.0×10^9) for electrochemical steps, which approximately captures the effect of solvent rearrangements at metal/H_2O interface during the proton-electron transfer[27]. The potential dependence of the $G_{a,i}$ is described as:

$$G_{a,i}(U_i) = \, G_{a,i}(U_i^o) + \beta e(U_i - U_i^o)$$

where β is a symmetric factor, which was assumed to be 0.5. The U_i and U_i^o are the applied electrode potential and the equilibrium potential of the corresponding electrochemical step, respectively, and $G_{a,i}(U_i)$ and $G_{a,i}(U_i^o)$ are activation energies at those potentials. We assumed that $G_{a,i}$ of all electrochemical steps are equivalent at their equilibrium potentials, following the simple reversible potential model by Hansen *et al.*, *i.e.*, $G_{a,i}(U_i^o) = G_a(U^o)$[27]. In this theoretical framework, we used 0.3 eV of the constant activation energy for deprotonation steps[28].

3. Results and Discussions

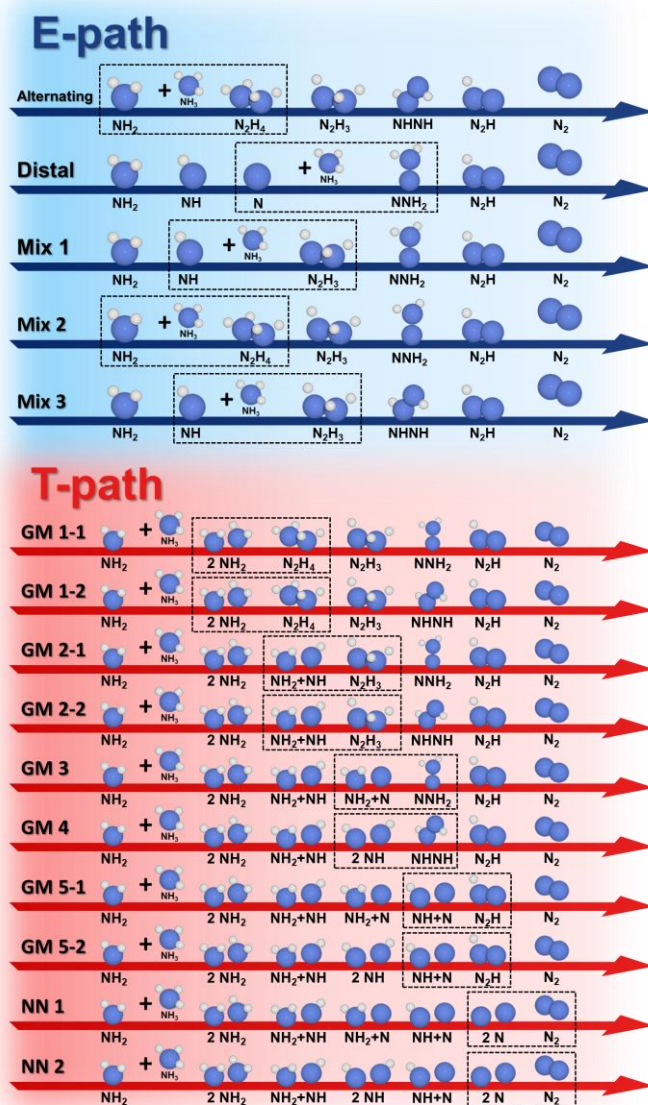## 3.1. Thermodynamic Limiting Potentials and Coupling Barriers

Figure 1. All possible reaction pathways for AOR. Electrochemical pathways (E-path) involve N-N coupling through the electrochemical deprotonation processes, while thermochemical pathways (T-path) involve GM and NN mechanisms. The coupling steps are highlighted with black dashed rectangles. Color code: Blue (N) and white (H).

A general approach to computationally investigate catalytic activities of electrocatalysts is to calculate the limiting potential (U_L), defined as the minimum potential to make all reaction steps downhill in the case of oxidation reactions[29, 30]. In this computational framework, electrochemical (de)protonation barriers are usually assumed to be surmountable (< 0.7 eV at 298 K) when U_L is applied, as evidenced by qualitative agreements between computational and experimental results for various electrochemical reactions[31]. This purely thermodynamic approach has been proved to be successful in reproducing experimental results and useful for providing catalyst design strategies[32-37].

When bond formations or dissociations through adsorbates are involved, however, merely U_L cannot be used to predict catalytic activities, since those processes are potential-independent[38, 39]. Therefore, it is essential to perform the microkinetic analysis to estimate TOFs by considering both thermodynamic/kinetic aspects and effects of the electrode potential. Although thermochemical coupling processes including GM ($NH_x^* + NH_y^* \rightarrow N_2H_{x+y}^*$) and NN ($N^* + N^* \rightarrow N_2^*$) mechanisms have mainly been investigated in literature, N-N coupling through electrochemical NH_3 deprotonation could also take place similar to the analogous process in OER, *i.e.,* $O^* + H_2O \rightarrow OOH^* + (H^+ + e^-)$[40]. Thus, we additionally included electrochemical coupling processes between adsorbed NH_x^* and NH_3 molecule, *i.e.,* $NH_x^* + NH_3 \rightarrow N_2H_{x+2}^* + (H^+ + e^-)$, in the microkinetic modeling. Note the electrochemical N-N bond formation involving deprotonations are potential-dependent. The reaction pathways containing thermochemical and electrochemical bond formations will be referred to as "T-path" and "E-path", respectively, hereafter. In total, we investigated 15 reaction pathways (**Figure 1**). In the following, we demonstrate the limitations of the purely thermodynamic approach, and discuss

results of the quantitative microkinetic analysis. Finally, we construct a kinetic volcano plot and propose a design strategy for an improved catalytic activity.
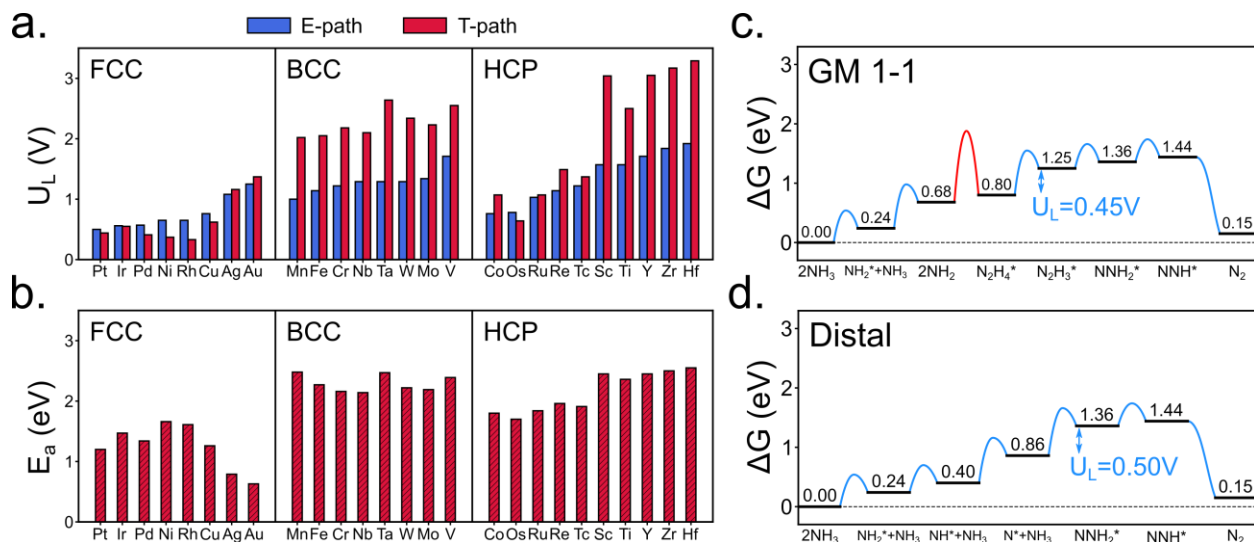

Figure 2. (a) The lowest U_L among all possible E-path (blue) and T-path (red). (b) The lowest $G_{a,i}$ of thermochemical N-N bond formation steps in T-path. Free energy diagrams of two representative reaction pathways on Pt (111), (c) GM 1-1 mechanism (T-path) and (d) distal mechanism (E-path). Red and blue lines correspond to barriers of thermochemical coupling ($G_{a,i}$ = 1.2 eV) and electrochemical deprotonation steps ($G_{a,i}$ = 0.3 eV at their equilibrium potentials), respectively.

By calculating U_L for all reaction pathways, we summarized the lowest U_L and the lowest $G_{a,i}$ (**Figure 2**, **Table S2-4**). It is clear that FCC metals with the exception of coinage metals (Ag, Au and Cu) demonstrated lower U_L than BCC or HCP metals for both E-path and T-path (**Figure 2a**). Particularly, Pt and Ir (Rh, Ni and Pd) exhibited the lowest U_L for E-path (T-path). On the other hand, the coinage metals showed higher U_L although their activation energies

in T-path are comparatively lower than the other FCC metals (**Figure 2b**). BCC metals generally featured higher U_L and activation energies than FCC and HCP metals, thus they are expected to be not appropriate for AOR. Among HCP metals, Co, Os and Ru demonstrated moderate U_L although their activation energies are relatively higher than FCC metals which have similar U_L. From this analysis, one could expect that FCC metals are more active than BCC and HCP metals in general, but it is inconclusive which metal is most active and a catalyst design strategy cannot be established on this basis.

As an additional example, we constructed free energy diagrams of two representative pathways on Pt (111); "GM 1-1" mechanism with the most facile N-N coupling step among T-path (**Figure 2c**) and "Distal" mechanism with the lowest U_L among E-path (**Figure 2d**). The calculated U_L for those pathways are 0.45 V and 0.50 V, respectively, suggesting that the former is thermodynamically more favorable. Since the thermochemical coupling barrier (1.2 eV) in GM 1-1 mechanism is larger and potential-independent, while the electrochemical counterpart in Distal mechanism is smaller and potential-dependent, however, one should perform more quantitative microkinetic analysis to compare the preference of mechanisms. This would also help to provide a catalyst design strategy, enabling *in silico* catalyst discovery.
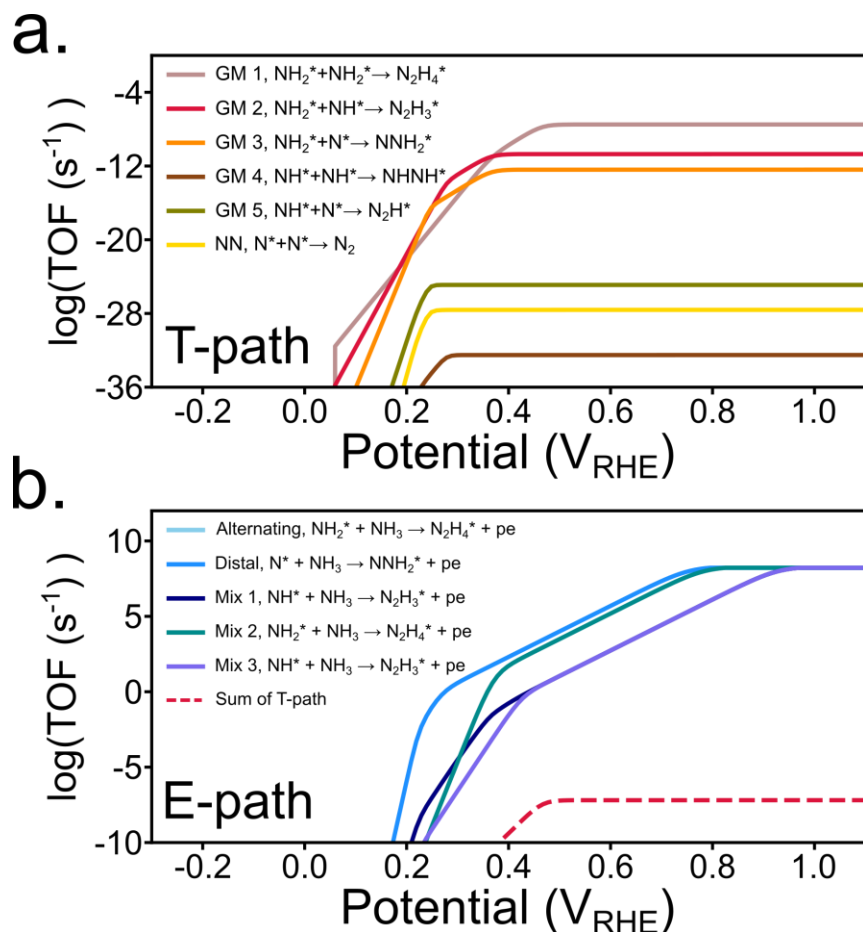
Figure 3. The calculated TOF of (a) T-path and (b) E-path from the microkinetic modeling for Pt (111). A sum of TOF for all T-path is presented as a red dashed curve in (b) for comparison. The corresponding N-N coupling step for each pathway is presented, where 'pe' indicates a proton and electron pair.

3.2. Microkinetic Analysis

The kinetic model was built based on all reaction pathways presented in **Figure 1**. We initially investigated a contribution of each pathway to the total TOF for Pt (111). Assuming the constant deprotonation barrier of 0.3 eV at the equilibrium potential of each electrochemical

step[28], we estimated TOF of each reaction pathway. In the case of T-path, the calculated TOFs of GM mechanisms are much more significant than NN mechanism (**Figure 3a**), in agreement with the conclusion of the previous work[9]. This is because the N-N bond formation step in T-path are potential-independent, thus lower activation energies in GM mechanisms led to higher TOF. For example, among GM mechanisms, TOF of GM 1 ($NH_2^* + NH_2^* \rightarrow N_2H_4^*$, $G_{a,i}$ = 1.20 eV) was much greater compared to GM 4 ($NH^* + NH^* \rightarrow N_2H_2^*$, $G_{a,i}$ = 2.69 eV) due to more facile bond formation of the former. For all the other metals, similar trends were observed, indicating that TOF of T-path is determined mainly by the activation energies of N-N bond formation steps (**Table S5**).

It is interesting to note that the sum of all TOFs of T-path was negligible compared to E-path (**Figure 3b**). In addition, TOF of T-path reached a plateau at potential close to U_L of Pt (111), while that of E-path increased until the potential increases up to 1.0 V_{RHE}. This could be attributed to potential-dependent deprotonation barriers, where increasing potential keeps decreasing those barriers, thus increasing the TOFs. These results suggest that E-path contributes more significantly to AOR compared to T-path and highlight that the electrochemical N-N bond formation steps should be included in the microkinetic modeling. Notably, we observed that the total TOF are highly correlated with the minimum value of U_L among all E-path, suggesting that this can be used as a descriptor for predicting the overall AOR activity (**Figure S4**). Since there is an uncertainty on electrochemical coupling barriers, we also tested 0.6 eV of $G_{a,i}$ for N-N bond formation steps[40], but similar trends were observed (**Figure S5**). Although this is beyond the scope of this work, these electrochemical bond formation barriers should be calculated in the future considering explicit water molecules and a constant potential scheme[41, 42].
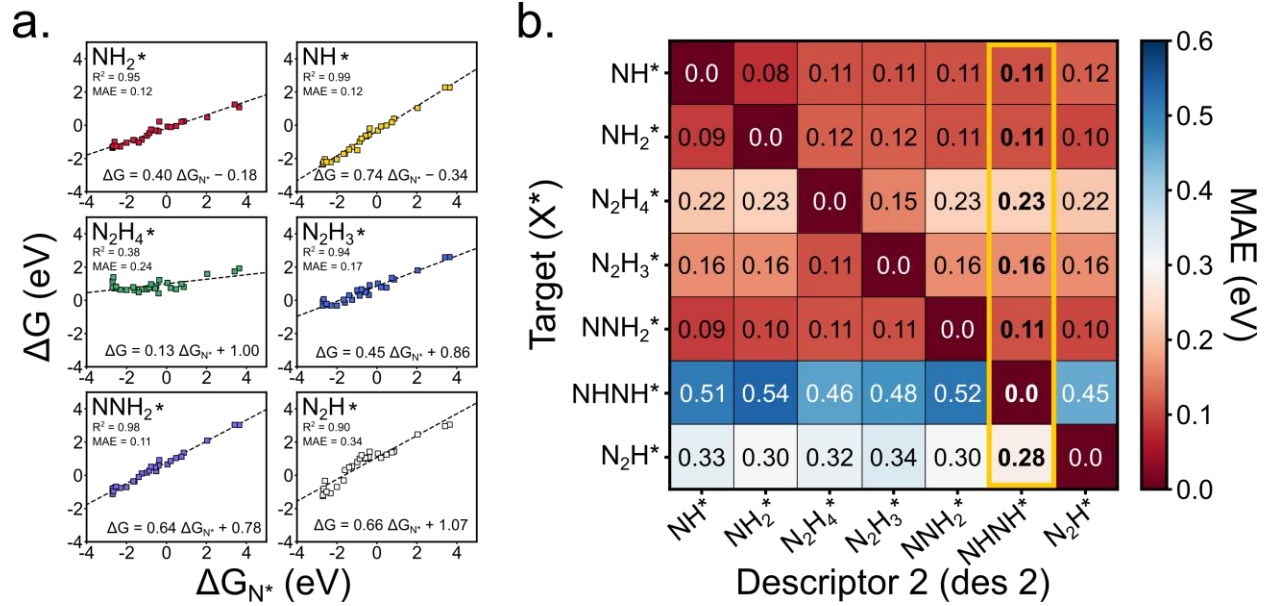
Figure 4. (a) Scaling relations between binding free energies of N* (ΔG_{N*}) and other adsorbates. (b) A matrix of MAEs between the predicted and the calculated binding free energies based on linear functions of ΔG_{N*} (*des 1*) and ΔG_{X*} (*des 2*). ΔG_{NHNH*} was chosen as *des 2*, which resulted in the smallest average MAE.

Since various reaction pathways are involved in AOR, developing simple descriptors would be beneficial for efficiently predicting catalytic activities and providing a catalyst design strategy[43, 44]. To reduce a dimensionality of reaction networks of AOR, we expressed binding free energies of reaction intermediates in the following linear functions,

$$\Delta G_{X*} = \alpha * \Delta G_{des\,1} + \beta * \Delta G_{des\,2} + \gamma$$

where ΔG_{X*}, ΔG_{des1} and ΔG_{des2} correspond to binding free energies of adsorbate X*, descriptor 1 (*des 1*) and 2 (*des 2*), respectively. α, β and γ are weights for *des 1* and *des 2*, and an intercept, respectively. ΔG_{N*} was chosen as the first descriptor, which is strongly correlated with binding

free energies of other adsorbates, except NHNH* (**Figure 4a, Figure S6**). To choose the second descriptor, we calculated mean absolute errors (MAEs) between the predicted binding free energies from the linear functions and the calculated ones. NHNH* is chosen as the second descriptor, which demonstrated the smallest average MAE for predicting binding free energies of the remaining adsorbates (**Figure 4b**, **Figure S7**). This could be due to the weakest correlation between ΔG_{N*} and ΔG_{NHNH*} (**Figure S6**).[45-49]

Based on the scaling relations and the BEP relations, we constructed a two-dimensional volcano plot, which predicts the total TOF using two simple descriptors (ΔG_{N*} and ΔG_{NHNH*}) (**Figure 5**). In line with the results of the thermodynamic analysis (**Figure 2**), BCC and HCP metals are suggested to be inactive due to too strong N* binding, while most of FCC metals, especially Pt, are predicted to be more active as they are located close to the top of the volcano.[16] Notably, Ag, Au and Cu are positioned at weakly N* binding region and expected to be inert, in agreement with the experimental results[16]. These agreements provide a reasonable rationale for using the microkinetic model and the volcano plot to understand the limitations of transition metal catalysts and to design new ones by overcoming those challenges.
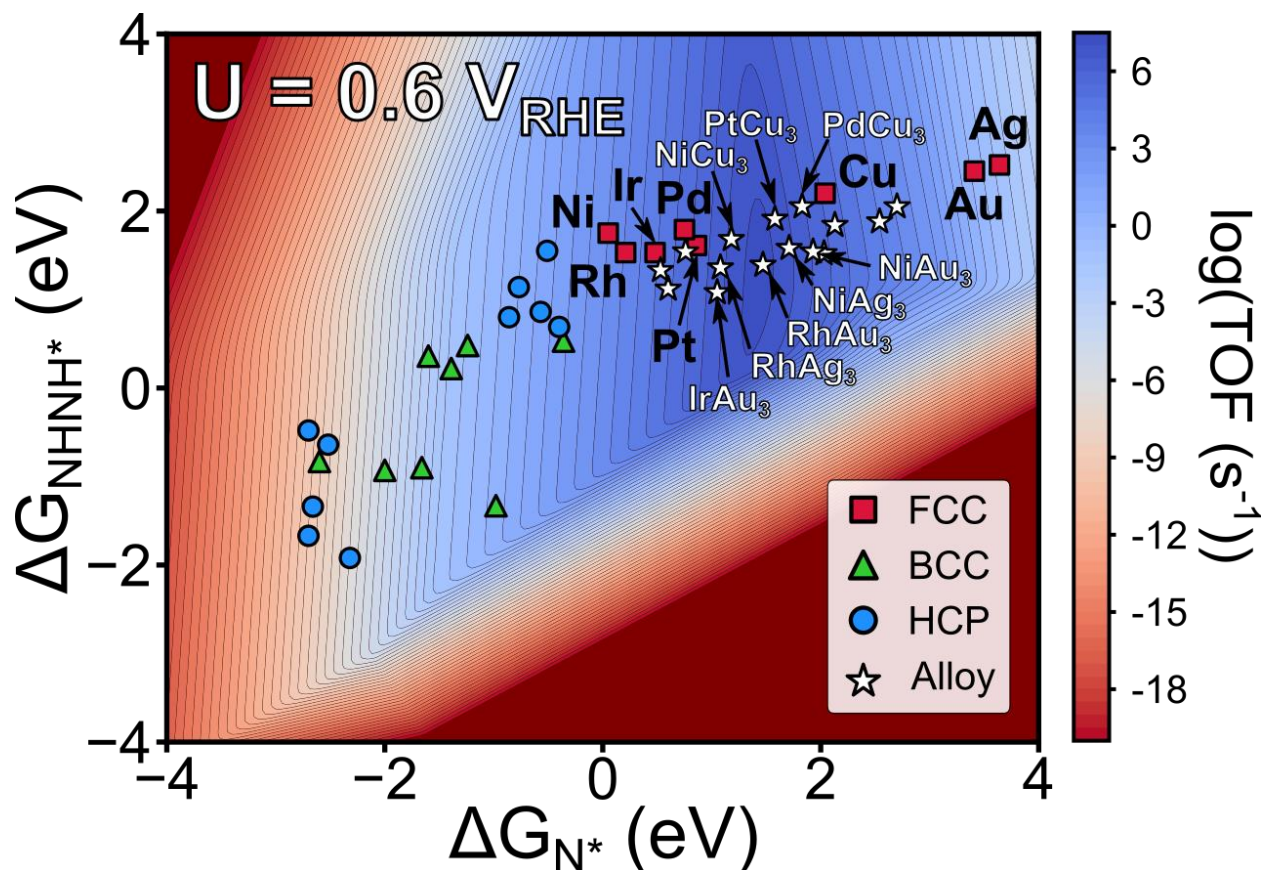
Figure 5. Two-dimensional volcano plot to predict the total TOF using two descriptors (ΔG_{N*} and ΔG_{NHNH*}). The applied potential was set to 0.60 V_{RHE}, which yielded the maximum current density for Pt catalyst.[16] Only FCC metals are highlighted for clarity, but the complete version can be found in **Figure S8**. We additionally tested the effect of higher $G_{a,i}$, which did not affect the overall conclusion (**Figure S9**).

3.3. Catalyst Design Strategy

It is clear from the volcano that fine-tuning ΔG_{N*} would be helpful to improve the catalytic activity as a change of TOF in the horizontal direction is more significant (**Figure 5**). Thus, one should focus on designing new catalysts of which ΔG_{N*} lies between Pt and Cu. One

approach to achieve this goal is to alloy metals with opposite N-affinities[50]. To validate this design strategy, we modeled (111) surface of various AB_3 alloys and calculated their ΔG_{NHNH*} and ΔG_{N*}, where A (=Pt, Pd, Ir, Ni, Rh) has stronger N-affinity than B (Ag, Au, Cu) (**Figure S10, Table S6**). Among 15 alloy combinations, 8 alloys ($IrAu_3$, $RhAg_3$, $NiCu_3$, $RhAu_3$, $PtCu_3$, $NiAg_3$, $PdCu_3$ and $NiAu_3$) are predicted to have larger TOF compared to their constituent metals and Pt. We note that AB_3 alloys have isolated "A" sites, preventing the thermochemical N-N coupling steps since active metal atoms are separated. As the contribution of E-path is much more significant on the metal catalysts, we expect the constructed kinetic volcano be valid for alloys as well.

4. Conclusions

In summary, we investigated catalytic activity trends of AOR on 26 *d*-block transition metals using DFT calculations and microkinetic modeling. By including the electrochemical bond formation steps in the microkinetic modeling, we enabled the quantitative comparison of various mechanisms and catalysts. Combined with the scaling relations, BEP relations and the microkinetic modeling, we constructed the kinetic volcano plot to predict TOF of catalysts using binding energies of two adsorbates as descriptors. The volcano plot suggested the catalyst design strategy to combine two elements with the opposite N-affinities, and we found a few candidates after performing the computational screening based on this strategy. Our study would provide the fundamental understanding of AOR and the basis of developing new active catalysts.

ASSOCIATED CONTENT

Supporting Information.

The following files are available free of charge on the ACS Publications website.

Further computational details. Atomic slab structures of transition metals and alloys. Two-dimensional volcano plots and the calculated TOFs of each reaction pathway. (PDF)

AUTHOR INFORMATION

Corresponding Author

Seoin Back − Department of Chemical and Biomolecular Engineering, Institute of Emergent Materials, Sogang University, Seoul 04107, Republic of Korea; Email: sback@sogang.ac.kr

Author

Ho Yeon Jang − Department of Chemical and Biomolecular Engineering, Institute of Emergent Materials, Sogang University, Seoul 04107, Republic of Korea

REFERENCES

(1) Pivovar, B.; Rustagi, N.; Satyapal, S. Hydrogen at scale (H2@ Scale): key to a clean, economic, and sustainable energy system. *Electrochem Soc Interface* **2018**, *27* (1), 47.

(2) Kannah, R. Y.; Kavitha, S.; Karthikeyan, O. P.; Kumar, G.; Dai-Viet, N. V.; Banu, J. R. Techno-economic assessment of various hydrogen production methods–A review. *Bioresour. Technol.* **2021**, *319*, 124175.

(3) Dou, B.; Zhang, H.; Song, Y.; Zhao, L.; Jiang, B.; He, M.; Ruan, C.; Chen, H.; Xu, Y. Hydrogen production from the thermochemical conversion of biomass: issues and challenges. *Sustain. Energy Fuels* **2019**, *3* (2), 314-342.

(4) Safari, F.; Dincer, I. A review and comparative evaluation of thermochemical water splitting cycles for hydrogen production. *Energy Convers. Manag.* **2020**, *205*, 112182.

(5) Divanis, S.; Kutlusoy, T.; Boye, I. M. I.; Man, I. C.; Rossmeisl, J. Oxygen evolution reaction: a perspective on a decade of atomic scale simulations. *Chem. Sci.* **2020**, *11* (11), 2943-2950.

(6) Cherevko, S.; Geiger, S.; Kasian, O.; Kulyk, N.; Grote, J.-P.; Savan, A.; Shrestha, B. R.; Merzlikin, S.; Breitbach, B.; Ludwig, A. Oxygen and hydrogen evolution reactions on Ru, RuO2, Ir, and IrO2 thin film electrodes in acidic and alkaline electrolytes: A comparative study on activity and stability. *Catal.* **2016**, *262*, 170-180.

(7) Zhong, C.; Hu, W.; Cheng, Y. Recent advances in electrocatalysts for electro-oxidation of ammonia. *J. Mater. Chem. A* **2013**, *1* (10), 3216-3238.

(8) Katsounaros, I.; Figueiredo, M. C.; Calle-Vallejo, F.; Li, H.; Gewirth, A. A.; Markovic, N. M.; Koper, M. T. On the mechanism of the electrochemical conversion of ammonia to dinitrogen on Pt (1 0 0) in alkaline environment. *J. Catal* **2018**, *359*, 82-91.

(9) Herron, J. A.; Ferrin, P.; Mavrikakis, M. Electrocatalytic oxidation of ammonia on transition-metal surfaces: a first-principles study. *J. Phys. Chem. C* **2015**, *119* (26), 14692-14701.

(10) Katan, T.; Galiotto, R. Current efficiencies for the anodic oxidation of ammonia in potassium hydroxide solution. *J. Electrochem. Soc.* **1963**, *110* (9), 1022.

(11) Simons, E.; Cairns, E.; Surd, D. The performance of direct ammonia fuel cells. *J. Electrochem. Soc.* **1969**, *116* (5), 556.

(12) Vidal-Iglesias, F.; García-Aráez, N.; Montiel, V.; Feliu, J.; Aldaz, A. Selective electrocatalysis of ammonia oxidation on Pt (1 0 0) sites in alkaline medium. *Electrochem. commun.* **2003**, *5* (1), 22-26.

(13) Vitse, F.; Cooper, M.; Botte, G. G. On the use of ammonia electrolysis for hydrogen production. *J. Power Sources* **2005**, *142* (1-2), 18-26.

(14) Zhou, L.; Cheng, Y. Catalytic electrolysis of ammonia on platinum in alkaline solution for hydrogen generation. *Int. J. Hydrog. Energy* **2008**, *33* (21), 5897-5904.

(15) Moran, E.; Cattaneo, C.; Mishima, H.; De Mishima, B. L.; Silvetti, S.; Rodriguez, J.; Pastor, E. Ammonia oxidation on electrodeposited Pt–Ir alloys. *J. Solid State Electrochem* **2008**, *12* (5), 583-589.

(16) De Vooys, A.; Koper, M.; Van Santen, R.; Van Veen, J. The role of adsorbates in the electrochemical oxidation of ammonia on noble and transition metal electrodes. *J. Electroanal. Chem.* **2001**, *506* (2), 127-137.

(17) Gerischer, H.; Mauerer, A. Untersuchungen zur anodischen oxidation von ammoniak an platin-elektroden. *J. Electroanal. Chem.* **1970**, *25* (3), 421-433.

(18) Elnabawy, A. O.; Herron, J. A.; Karraker, S.; Mavrikakis, M. Structure sensitivity of ammonia electro-oxidation on transition metal surfaces: A first-principles study. *J. Catal* **2021**, *397*, 137-147.

(19) Kresse, G.; Hafner, J. Ab initio molecular dynamics for open-shell transition metals. *Phys. Rev. B Condens. Matter* **1993**, *48* (17), 13115.

(20) Kresse, G.; Furthmüller, J. Efficiency of ab-initio total energy calculations for metals and semiconductors using a plane-wave basis set. *Comput. Mater. Sci.* **1996**, *6* (1), 15-50.

(21) Wellendorff, J.; Lundgaard, K. T.; Møgelhøj, A.; Petzold, V.; Landis, D. D.; Nørskov, J. K.; Bligaard, T.; Jacobsen, K. W. Density functionals for surface science: Exchange-correlation model development with Bayesian error estimation. *Phys. Rev. B Condens. Matter* **2012**, *85* (23), 235149.

(22) Monkhorst, H. J.; Pack, J. D. Special points for Brillouin-zone integrations. *Phys. Rev. B Condens. Matter* **1976**, *13* (12), 5188.

(23) Nørskov, J. K.; Rossmeisl, J.; Logadottir, A.; Lindqvist, L.; Kitchin, J. R.; Bligaard, T.; Jonsson, H. Origin of the overpotential for oxygen reduction at a fuel-cell cathode. *J. Phys. Chem. B* **2004**, *108* (46), 17886-17892.

(24) Larsen, A. H.; Mortensen, J. J.; Blomqvist, J.; Castelli, I. E.; Christensen, R.; Dułak, M.; Friis, J.; Groves, M. N.; Hammer, B.; Hargus, C. The atomic simulation environment—a Python library for working with atoms. *J. Condens. Matter Phys.* **2017**, *29* (27), 273002.

(25) Mathew, K.; Sundararaman, R.; Letchworth-Weaver, K.; Arias, T.; Hennig, R. G. Implicit solvation model for density-functional study of nanocrystal surfaces and reaction pathways. *J. Chem. Phys.* **2014**, *140* (8), 084106.

(26) Medford, A. J.; Shi, C.; Hoffmann, M. J.; Lausche, A. C.; Fitzgibbon, S. R.; Bligaard, T.; Nørskov, J. K. CatMAP: a software package for descriptor-based microkinetic mapping of catalytic trends. *Catal. Lett.* **2015**, *145* (3), 794-807.

(27) Hansen, H. A.; Viswanathan, V.; Nørskov, J. K. Unifying kinetic and thermodynamic analysis of 2 e–and 4 e–reduction of oxygen on metal surfaces. *J. Phys. Chem. C* **2014**, *118* (13), 6706-6718.

(28) Sa, Y. J.; Jung, H.; Shin, D.; Jeong, H. Y.; Ringe, S.; Kim, H.; Hwang, Y. J.; Joo, S. H. Thermal transformation of molecular Ni2+–N4 sites for enhanced CO2 electroreduction activity. *ACS Catal.* **2020**, *10* (19), 10920-10931.

(29) Peterson, A. A.; Abild-Pedersen, F.; Studt, F.; Rossmeisl, J.; Nørskov, J. K. How copper catalyzes the electroreduction of carbon dioxide into hydrocarbon fuels. *Energy Environ. Sci.* **2010**, *3* (9), 1311-1315.

(30) Back, S.; Jung, Y. On the mechanism of electrochemical ammonia synthesis on the Ru catalyst. *Phys. Chem. Chem. Phys.* **2016**, *18* (13), 9161-9166.

(31) Seh, Z. W.; Kibsgaard, J.; Dickens, C. F.; Chorkendorff, I.; Nørskov, J. K.; Jaramillo, T. F. Combining theory and experiment in electrocatalysis: Insights into materials design. *Science* **2017**, *355* (6321).

(32) Peterson, A. A.; Nørskov, J. K. Activity descriptors for CO2 electroreduction to methane on transition-metal catalysts. *J. Phys. Chem. Lett* **2012**, *3* (2), 251-258.

(33) Kulkarni, A.; Siahrostami, S.; Patel, A.; Nørskov, J. K. Understanding catalytic activity trends in the oxygen reduction reaction. *Chem. Rev.* **2018**, *118* (5), 2302-2312.

(34) Howalt, J. G.; Bligaard, T.; Rossmeisl, J.; Vegge, T. DFT based study of transition metal nano-clusters for electrochemical NH 3 production. *Phys. Chem. Chem. Phys.* **2013**, *15* (20), 7785-7795.

(35) Arnarson, L.; Schmidt, P. S.; Pandey, M.; Bagger, A.; Thygesen, K. S.; Stephens, I. E.; Rossmeisl, J. Fundamental limitation of electrocatalytic methane conversion to methanol. *Phys. Chem. Chem. Phys.* **2018**, *20* (16), 11152-11159.

(36) Durand, W. J.; Peterson, A. A.; Studt, F.; Abild-Pedersen, F.; Nørskov, J. K. Structure effects on the energetics of the electrochemical reduction of CO2 by copper surfaces. *Surf. Sci.* **2011**, *605* (15-16), 1354-1359.

(37) Xu, C.; Zhi, X.; Vasileff, A.; Wang, D.; Jin, B.; Jiao, Y.; Zheng, Y.; Qiao, S.-Z. Highly Selective Two-Electron Electrocatalytic CO2 Reduction on Single-Atom Cu Catalysts. *Small Structures* **2021**, *2* (1), 2000058.

(38) Tripković, V.; Skúlason, E.; Siahrostami, S.; Nørskov, J. K.; Rossmeisl, J. The oxygen reduction reaction mechanism on Pt (1 1 1) from density functional theory calculations. *Electrochim. Acta* **2010**, *55* (27), 7975-7981.

(39) Chan, K.; Nørskov, J. K. Potential dependence of electrochemical barriers from ab initio calculations. *J. Phys. Chem. Lett* **2016**, *7* (9), 1686-1690.

(40) Dickens, C. F.; Kirk, C.; Nørskov, J. K. Insights into the electrochemical oxygen evolution reaction with ab initio calculations and microkinetic modeling: beyond the limiting potential volcano. *J. Phys. Chem. C* **2019**, *123* (31), 18960-18977.

(41) Gauthier, J. A.; Dickens, C. F.; Chen, L. D.; Doyle, A. D.; Nørskov, J. K. Solvation effects for oxygen evolution reaction catalysis on IrO2 (110). *J. Phys. Chem. C* **2017**, *121* (21), 11455-11463.

(42) Chan, K.; Nørskov, J. K. Electrochemical barriers made simple. *J. Phys. Chem. Lett* **2015**, *6* (14), 2663-2668.

(43) Wang, Y.; Yang, X.; Xiao, L.; Qi, Y.; Yang, J.; Zhu, Y.-A.; Holmen, A.; Xiao, W.; Chen, D. Descriptor-Based Microkinetic Modeling and Catalyst Screening for CO Hydrogenation. *ACS Catal.* **2021**, *11*, 14545-14560.

(44) Xiao, L.; Hu, P.; Sui, Z.-J.; Chen, D.; Zhou, X.-G.; Yuan, W.-K.; Zhu, Y.-A. Rational design of intermetallic compound catalysts for propane dehydrogenation from a descriptor-based microkinetic analysis. *J. Catal* **2021**, *404*, 32-45.

(45) Wang, Y.; Xiao, L.; Qi, Y.; Yang, J.; Zhu, Y.-A.; Chen, D. Insight into Size-and Metal-Dependent Activity and the Mechanism for Steam Methane Re-forming in Nanocatalysis. *J. Phys. Chem. C* **2020**, *124* (4), 2501-2512.

(46) Jones, G.; Jakobsen, J. G.; Shim, S. S.; Kleis, J.; Andersson, M. P.; Rossmeisl, J.; Abild-Pedersen, F.; Bligaard, T.; Helveg, S.; Hinnemann, B. First principles calculations and experimental insight into methane steam reforming over transition metal catalysts. *J. Catal* **2008**, *259* (1), 147-160.

(47) Yoo, J. S.; Schumann, J.; Studt, F.; Abild-Pedersen, F.; Nørskov, J. K. Theoretical investigation of methane oxidation on Pd (111) and other metallic surfaces. *J. Phys. Chem. C* **2018**, *122* (28), 16023-16032.

(48) Jalid, F.; Khan, T. S.; Haider, M. A. CO 2 reduction and ethane dehydrogenation on transition metal catalysts: mechanistic insights, reactivity trends and rational design of bimetallic alloys. *Catal. Sci. Technol.* **2021**, *11* (1), 97-115.

(49) Hansen, M. H.; Nørskov, J. K.; Bligaard, T. First principles micro-kinetic model of catalytic non-oxidative dehydrogenation of ethane over close-packed metallic facets. *J. Catal* **2019**, *374*, 161-170.

(50) dos Santos, E. C.; Araujo, R. B.; Valter, M.; Salazar-Alvarez, G.; Johnsson, M.; Bajdich, M.; Abild-Pedersen, F.; Pettersson, L. G. M. Efficient Screening of Bi-Metallic Electrocatalysts for Glycerol Valorization. *Electrochim. Acta* **2021**, 139283.

TOF Figure